J. Fluid Mech. (2008), *vol.* 615, *pp.* 139–167. © 2008 Cambridge University Press
doi:10.1017/S0022112008003613 Printed in the United Kingdom

A unified framework for nonlinear combustion instability analysis based on the flame describing function

N. NOIRAY, D. DUROX, T. SCHULLER AND S. CANDEL

Ecole Centrale Paris, EM2C Laboratory, CNRS, 92295 Châtenay-Malabry, France

(Received 6 March 2008 and in revised form 8 July 2008)

Analysis of combustion instabilities relies in most cases on linear analysis but most observations of these processes are carried out in the nonlinear regime where the system oscillates at a limit cycle. The objective of this paper is to deal with these two manifestations of combustion instabilities in a unified framework. The flame is recognized as the main nonlinear element in the system and its response to perturbations is characterized in terms of generalized transfer functions which assume that the gain and phase depend on the amplitude level of the input. This 'describing function' framework implies that the fundamental frequency is predominant and that the higher harmonics generated in the nonlinear element are weak because the higher frequencies are filtered out by the other components of the system. Based on this idea, a methodology is proposed to investigate the nonlinear stability of burners by associating the flame describing function with a frequency-domain analysis of the burner acoustics. These elements yield a nonlinear dispersion relation which can be solved, yielding growth rates and eigenfrequencies, which depend on the amplitude level of perturbations impinging on the flame. This method is used to investigate the regimes of oscillation of a well-controlled experiment. The system includes a resonant upstream manifold formed by a duct having a continuously adjustable length and a combustion region comprising a large number of flames stabilized on a multipoint injection system. The growth rates and eigenfrequencies are determined for a wide range of duct lengths. For certain values of this parameter we find a positive growth rate for vanishingly small amplitude levels, indicating that the system is linearly unstable. The growth rate then changes as the amplitude is increased and eventually vanishes for a finite amplitude, indicating the existence of a limit cycle. For other values of the length, the growth rate is initially negative, becomes positive for a finite amplitude and drops to zero for a higher value. This indicates that the system is linearly stable but nonlinearly unstable. Using calculated growth rates it is possible to predict amplitudes of oscillation when the system operates on a limit cycle. Mode switching and instability triggering may also be anticipated by comparing the growth rate curves. Theoretical results are found to be in excellent agreement with measurements, indicating that the flame describing function (FDF) methodology constitutes a suitable framework for nonlinear instability analysis.

1. Introduction

Research on combustion instabilities is quite intense worldwide but prediction of these processes at the design stage still constitutes a challenge. Instability problems affect a wide variety of systems ranging from domestic boilers to gas turbines for

https://doi.org/10.1017/S0022112008003613 Published online by Cambridge University Press

electricity and power generation, large thermal plants, ramjets and rocket engines. They cause structural vibrations, augmented heat fluxes to the chamber walls, reducing the system lifetime and often leading to severe damage. Combustion oscillations are particularly harmful for jet engines and in extreme cases lead to spectacular failures, unfortunately, these regimes of operation are promoted by new combustion technologies in which fuel and air are premixed before burning. These novel premixing systems lead to low levels of pollutant emissions but also favour combustion/acoustics interactions and are therefore susceptible to resonant coupling and instabilities (Lieuwen & Yang 2005). One central difficulty in the analysis of combustion instabilities in most practical systems is related to the nonlinear flame dynamics. Manifestations of these nonlinearities are well-documented on the basis of observations on laminar or turbulent flame configurations but there are fewer direct quantitative comparisons between experiments and theory. The theoretical interpretation is usually based on linear stability analysis in which one examines the growth rate of infinitesimally small perturbations, but in most cases experiments on self-sustained instabilities are carried out on systems which have reached a limit cycle at a finite level of oscillation. In some special cases it has been possible to measure the linear growth rate, for example by making use of active control methods (Poinsot *et al.* 1988, 1992) allowing a comparison between theory and experiment. But in most investigations the instability development cannot be controlled and a linear analysis is carried out to define the stability map. This has been applied to many simple experiments and more recently to practical configurations, taking into account their geometrical and flow complexities, as for example by Paschereit *et al.* (2002), Sattelmayer (2003), Krebs *et al.* (2005) or Roux *et al.* (2005). These studies include predictions of small-perturbation growth rates while experiments correspond to well-established oscillations. There is clearly a gap between theoretical results and experimental data. A relatively large number of studies however have tried to fill this gap and propose nonlinear descriptions of combustion instabilities.

In a first group of investigations, the focus has been on solid-propellant rocket engines and on developments of nonlinear acoustics to describe the non-steady gasdynamics. These studies are based on expansions of the acoustic eigenmodes such as initially introduced by Zinn & Lores (1972). This framework has been extensively explored by Culick and coworkers mainly in relation to solid-propellant rockets. Typical examples of this approach provide an explanation of the saturation phenomenon observed when the oscillation reaches a limit cycle (Yang, Kim & Culick 1990; Culick 1994; Jahnke & Culick 1994; Burnley & Culick 1999). These studies remain in most cases essentially theoretical, probably because it is not easy to develop systematic experiments in this area. Much of this theoretical effort has focused on nonlinearities associated with gasdynamics while the nonlinear combustion dynamics are less well investigated. It has been pointed out by these authors that nonlinear acoustics could not provide an explanation of the nonlinear onset of instabilities designated as 'triggering'. A recent evolution has therefore consisted of establishing a nonlinear model for the solid-propellant response to derive conditions for triggering. This phenomenon is demonstrated theoretically by Culick, Burnley & Swenson (1995), Wicker *et al.* (1996) or Ananthkrishnan, Deo & Culick (2005).

A second group of studies is generally concerned with instabilities in gas turbine combustors and emphasizes the flame dynamics. It is indicated that many of the features of combustion instabilities are controlled by nonlinearities of the flame as underlined for example by Peracchio & Proscia (1999) or Lieuwen (2002). This is exemplified by experimental observations of saturation of heat release oscillations

https://doi.org/10.1017/S0022112008003613 Published online by Cambridge University Press

(e.g. Lieuwen & Neumeier 2002; Lee & Santavicca 2003; Balachandran *et al.* 2005; Bellows *et al.* 2007; Birbaud *et al.* 2007). The nonlinear flame dynamics has also been described theoretically with models of the unsteady flame motion (Poinsot & Candel 1988). The nonlinearity induced by flashback of a ducted flame is elegantly described in a model put forward by Dowling (1999). Nonlinear models which rely on the kinematic description of initially conical flames subjected to finite level perturbations have been developed by Lieuwen (2005). Simplified descriptions of the nonlinear gain of the flame are exploited by Dowling (1997) and various types of numerical simulations have been used to examine finite-amplitude motions (e.g. Armitage *et al.* 2006).

The present study belongs to a third group of investigations. The aim of that group is to include the nonlinear flame dynamics features in a complete combustion instability analysis. Notable are the works of Dowling (1997, 1999) and Morgans & Stow (2007). These references do not, however, contain the nonlinear description of the flame response delay – it is shown in the present paper that this is a key element – and are not supported by experimental validations. A nonlinear-heat-release acoustic model is proposed by Peracchio & Proscia (1999) to describe observations made in a representative model-scale combustor, but this application of nonlinear analysis features adjustment parameters and the experimental validation is limited because the test rig has a fixed geometry. Balasubramanian & Sujith (2008) have recently demonstrated theoretically that in the case of diffusion flames, such nonlinear onset can be analysed in the time domain by considering both the nonlinearity of the flame response and the nonnormality of the coupled eigenmodes.

Note also that other nonlinear interactions of parametric type can arise between a flame and its sound field when the front propagates downwards in premixed reactants confined in a tube (Searby & Rochwerger 1991 and Wu *et al.* 2003). This special type of nonlinear coupling linked to intrinsic instabilities differs from the system instabilities envisaged in the present article.

As indicated by Lawn, Evesque & Polifke (2004) and by many of the previously listed authors, further studies of the mechanisms of flame response are needed to understand the nonlinear combustion instability processes. The objective of the present paper is to develop one such analysis which may be employed to predict amplitudes of oscillation at the limit cycle and explain mode switching and instability triggering phenomena. More precisely, the aim is to (i) quantitatively predict limit cycles amplitude and frequencies, (ii) predict hysteresis phenomena, (iii) determine frequency shifts during transients, (iv) explain finite-amplitude triggering and (v) give an explanation for the linear and nonlinear onset, and different processes leading to saturation.

The analysis is illustrated in a well-controlled experimental configuration (Noiray *et al.* 2006, 2007). A theoretical analysis of the thermoacoustic coupling has already been carried out from a linear point of view in these previous studies. The results provide suitable estimations of the unstable frequencies but the model does not explain how and why limit cycles are reached. Indeed, the linear representation predicts infinite growth of initial perturbations which is naturally not the case in practical systems.

A nonlinear analysis should be developed to account for saturation phenomena. This is accomplished here by making use of the describing function framework which is well-established in nonlinear control but less common in combustion dynamics studies (see Culick 2006, appendix H). The central idea is to define a flame transfer function which depends on both input frequency and amplitude. In this approach one assumes that the fundamental frequency determines the dynamics of the system while higher harmonics generated in the nonlinear process are of sufficiently low amplitude

https://doi.org/10.1017/S0022112008003613 Published online by Cambridge University Press

to have a negligible effect on the system stability. This can be so for a number of reasons: (i) the nonlinearity is weak, (ii) the higher harmonics are filtered out by the other components of the system, (iii) the fundamental conveys the major part of the power.

When the describing function is employed to represent the flame response it is possible to perform a frequency-domain analysis by solving the dispersion relation for a range of amplitudes. This nonlinear dispersion relation (NDR) yields growth rates and eigenfrequencies which depend on the amplitude level of perturbations impinging on the flame. This notably differs from the standard linear stability analysis which only yields constant growth rates and frequencies.

In the present study, the 'flame describing function' or FDF is used to systematically investigate regimes of oscillation of a well-controlled experiment. The system comprises a resonant upstream manifold formed by a duct having a continuously adjustable length to modify the burner acoustics. This approach will be shown to yield meaningful results. In one early investigation of combustion–acoustics coupling, Crocco, Grey & Harrje (1960) also used a chamber with a variable size in the context of rocket instabilities. In the present study, the combustion region is unconfined and comprises a large number of flames stabilized on a multipoint injection system. The adjustable duct length L is used as a bifurcation parameter to identify the various modes of oscillation and extract the system bifurcation diagram.

This paper begins with a brief presentation of the experimental setup. The instability analysis is reviewed and the dispersion relation is obtained. Flame transfer functions corresponding to different input levels are determined by subjecting the flames to acoustic perturbations and sweeping the frequency for a range of modulation amplitudes. This yields the flame describing function which is then inserted in the dispersion relation. This equation is solved, providing growth rates as a function of amplitude. Results obtained for different input levels are then used to predict limit-cycle amplitudes and compare these predictions with experimental data. The last section is concerned with mode switching and instability triggering. One case of mode transition is described in detail. It is shown that this phenomenon can be explained by examining the evolution of growth rates for the possible modes of resonance corresponding to a particular size of the upstream manifold. A bifurcation diagram is then proposed which synthesizes theoretical predictions and experimental observations.

2. Experimental setup and combustion regimes

The experimental layout is sketched in figure 1. The combustion zone (see figure 2) is unconfined and the thermo-acoustic coupling described here involves a feedback loop between a collection of flames and the upstream manifold. The three main elements of the burner are a perforated plate which serves to anchor the flames, a resonant cavity and a piston from which the premixture is injected. Such multipoint injection geometries are used in many applications (domestic boilers, drying systems, some novel gas turbine concepts, etc.). The head of the piston is flat providing a quasi-perfect acoustic reflection boundary at the bottom of the burner. It is easy to modify the resonant cavity size L (and thus the acoustic properties of the burner) by changing the piston position. The length L used in this investigation as a bifurcation parameter takes values from 10 to 75 cm. The resonant duct radius $R = 3.5$ cm is small enough to assume that wave propagation is longitudinal in the upstream duct for frequencies lower than 1500 Hz. At ambient conditions, the corresponding wavelengths $\lambda = c/f$ exceed 23 cm, which is much larger than the duct radius R.

https://doi.org/10.1017/S0022112008003613 Published online by Cambridge University Press

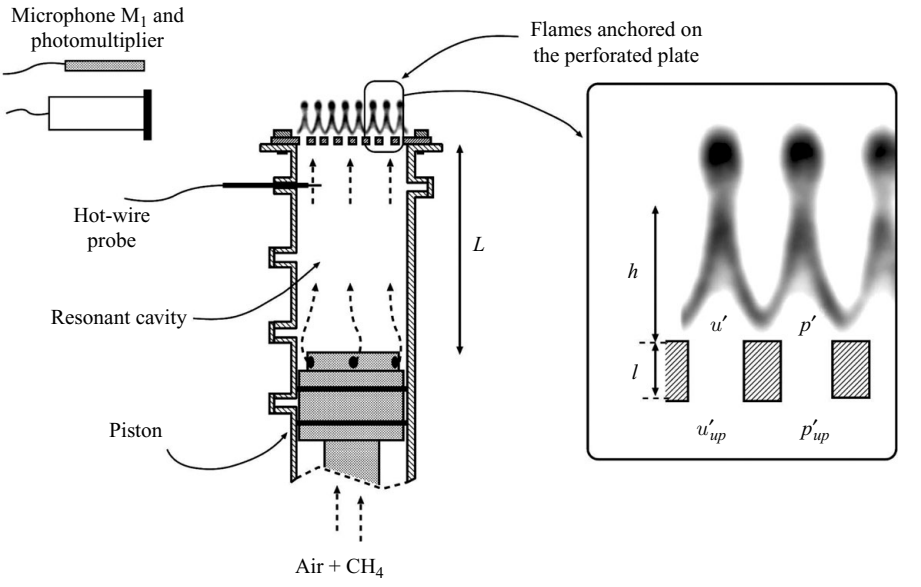


FIGURE 1. Experimental setup. The burner is sketched on the left. A close-up view of the flames anchored on the perforated plate is displayed on the right. Three quantities are measured in the present study: acoustic pressure by means of microphone M_1 placed 35 cm from the burner axis in the horizontal plane containing the perforated plate; OH^* light emission by means of a photomultiplier equipped with a bandpass filter; and flow velocity perturbation with a hot-wire probe mounted 2 cm below the perforated plate inside the manifold.

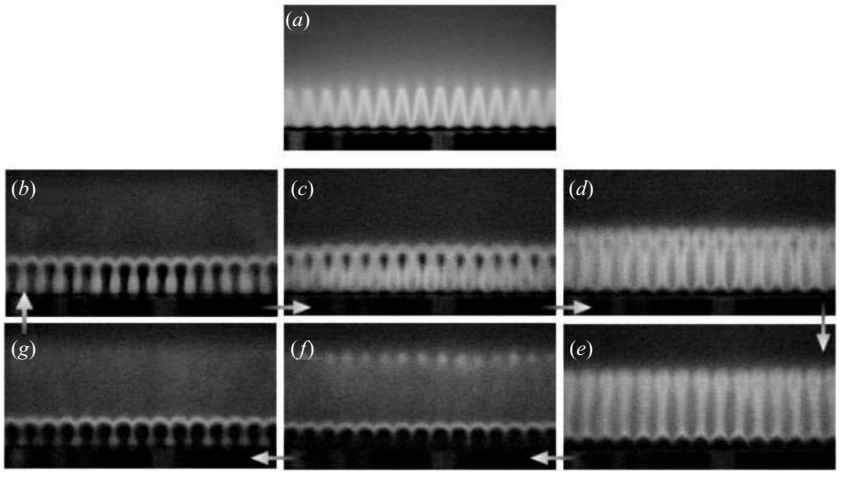


FIGURE 2. Instantaneous flame images taken from the side. (*a*) Stable combustion regime, cavity length $L = 26.4$ cm, radiated noise level 80 dB (Microphone M_1). (*b–g*) Unstable combustion regime. Six images are recorded during a cycle at regularly spaced instants. Cavity length $L = 46$ cm, oscillation frequency $f = 522$ Hz, radiated noise level 111 dB (Microphone M_1).

The premixed reactants flow from the piston to the perforated plate where reaction takes place. Volume flow rate and equivalence ratio are respectively fixed at 4.5×10^{-3} N m^3 s^{-1} and 0.86 providing a thermal power of 14 kW. The perforated plate made of stainless steel has a thickness $l = 3$ mm and comprises regularly distributed

https://doi.org/10.1017/S0022112008003613 Published online by Cambridge University Press

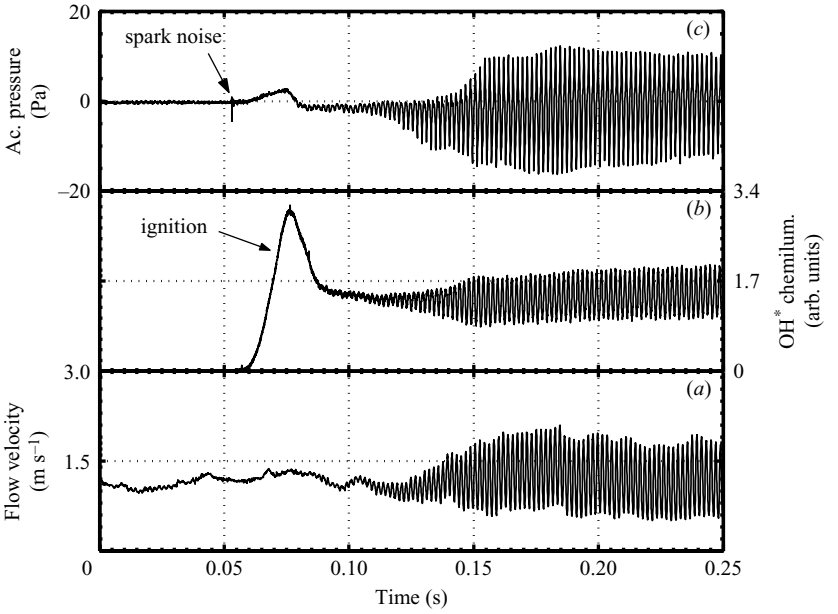


FIGURE 3. Temporal evolution of (*a*) the velocity, (*b*) OH^* light emission and (*c*) acoustic pressure, respectively recorded by an upstream hot-wire probe, a photomultiplier and microphone M_1 (see figure 1). The unstable combustion regime corresponds to a cavity size $L = 46$ cm and the oscillation frequency $f = 522$ Hz.

holes of radius $r_p = 1$ mm. Holes have been machined on a 3 mm square mesh and the plate features $N = 420$ perforations with a global porosity $P = N\pi r_p^2/\pi R^2$ of 0.34.

Combustion regimes are either 'stable' or 'unstable' depending on the duct size L. Stable regimes correspond to a steady mode of burning characterized by a low level of noise emission with individual flames taking classical conical shapes and remaining still (figure 2*a*). The noise level radiated by the system in this case is approximately 80 dB (reference pressure 2×10^{-5} Pa) measured by microphone M_1. Unstable regimes pertain to an oscillation of finite amplitude. A typical example is given in figure 2(*b–g*). The system operates in this case on a limit cycle (stable oscillatory state). In this unsteady mode, individual flame sheets periodically stretch and recoil at a frequency close to one of the burner acoustic eigenfrequencies. The case presented in figure 2 corresponds to an oscillating limit cycle obtained for a burner size $L = 46$ cm. In this situation, the frequency $f = 522$ Hz is close to the three-quarter wave eigenfrequency of the burner $3c/4L = 554$ Hz where $c = 340$ m s^{-1} designates the speed of sound in the fresh stream at ambient temperature. The flame-front oscillation is accompanied by an intense sound emission exceeding 110 dB at microphone M_1. This radiated sound is generated by the rapid fluctuations of the flame fronts during the oscillation cycle (figure 2*b–g*). The flame surface motion induces strong fluctuations of the volumetric gas expansion through the flames fronts, which act like a distribution of acoustic sources.

Time records of the different quantities measured in the present study are displayed in figure 3 for the unstable combustion regime obtained for $L = 46$ cm (see figure 2*b–g*). The flow velocity measured by the hot-wire probe placed 2 cm below the perforated plate (see figure 1) is plotted in figure 3(*a*). Light intensity radiated by OH^* radicals formed in the flame and acoustic pressure recorded by microphone M_1 are displayed

https://doi.org/10.1017/S0022112008003613 Published online by Cambridge University Press

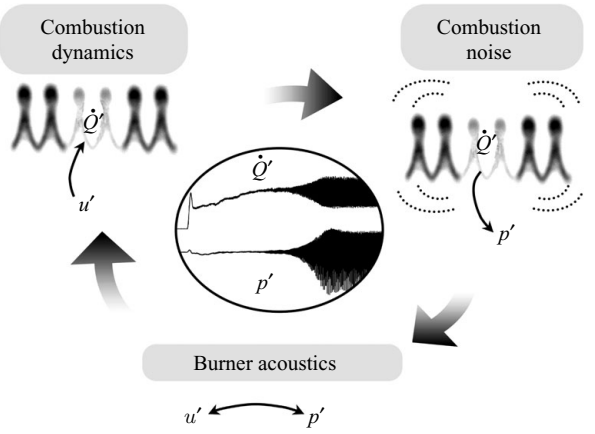


FIGURE 4. Qualitative representation of the resonant coupling mechanisms.

in figures 3(*b*) and 3(*c*). These signals are respectively detected by a photomultiplier equipped with a filter centred on the OH^* emission band around 308 nm and microphone M_1 placed 35 cm away from the burner axis. Combustion is ignited by a spark which produces a small impulse in the pressure signal in figure 3(*c*) at $t \simeq 0.06$ s. Ignition occurs with a burst of light from $t \simeq 0.06$ to $t \simeq 0.08$ s (see figure 3*b*). At that time, flames are well-anchored on the burner outlet and small oscillations of the acoustic pressure (figure 3*c*), OH^* light emission (figure 3*b*) and flow velocity inside the upstream manifold (figure 3*a*) begin to grow. It takes about 70 ms to reach the limit cycle at a relatively fast rate corresponding approximately to 40 periods. The saturation amplitude of the acoustic pressure is about $p'_{rms} = 6.9$ Pa which is equivalent to a sound pressure level of 111 dB ($SPL(dB) = 20\ \log_{10}(p'_{rms}/p_a)$ where $p_a = 2 \times 10^{-5}$ Pa is the reference pressure).

3. Analytical modelling

It is useful to derive an analytical model of the thermoacoustic coupling first, which can be used to retrieve experimental observations and will provide a basis for the nonlinear analysis. A qualitative description of the resonant coupling is put forward first. This is followed by analytical modelling of the main processes involved in the instability phenomenon. A dispersion relation is finally obtained by making use of these results. In this linear analysis, flow variables are written as sums of a mean and a fluctuating component $a = \bar{a} + a'$. In the frequency-domain analysis the fluctuating quantities are treated as harmonic perturbations and cast in the conventional form: $a' = |a'|e^{-i\omega t}$, where $\omega = \omega_r + i\omega_i$ denotes the complex angular frequency with $\omega_r = 2\pi f$ and ω_i respectively defining the angular frequency and the growth rate. For positive values of ω_i the perturbation grows, while it decays in the opposite case.

3.1. *Qualitative description of the thermo-acoustic instability*

The resonant coupling mechanism is represented schematically in figure 4. In the present configuration the flames move in response to upstream velocity fluctuations u' impinging on the flames as indicated on the left-hand side in the figure. These flow rate fluctuations affect the flame surface area, inducing heat release rate fluctuations $\dot{Q}'$. The flame response to incoming velocity perturbations has been extensively investigated in analyses of flame transfer functions. The resulting heat release rate

https://doi.org/10.1017/S0022112008003613 Published online by Cambridge University Press

fluctuations $\dot{Q}'$ induce unsteady gas expansion fluctuations which generate acoustic pressure oscillations p'. Combustion noise associated with this process is again well-documented in the literature. Pressure fluctuations are radiated over all space and in particular back to the upstream manifold through the perforated plate. This gives rise to a feedback effect which is sustained by the upstream duct resonance. This process links pressure p' and velocity u' fluctuations at the burner outlet.

The different mechanisms listed previously are now used to derive a dispersion relation which defines the system dynamics. The following derivation is based on the analysis proposed by Schuller, Durox & Candel (2003*a*) and Noiray *et al.* (2006). Note that the present work includes a more detailed description of the pressure field radiated by the flame collection than that presented by Noiray *et al.* (2006). In addition, the flame transfer function (FTF) will be replaced by the flame describing function (FDF) to provide a nonlinear description of the thermo-acoustic coupling.

3.2. *Burner acoustics*

In a first approximation, the burner may be treated as an acoustically open-ended tube. The piston offers a quasi-perfect rigid boundary and the perforated plate fixed at the top of the manifold barely modifies the system eigenfrequencies. In the low frequency range considered in this study only longitudinal waves propagate in the duct. The link between acoustic velocity u' and pressure fluctuations p' at the burner outlet is deduced from a classical analysis of duct acoustics (e.g. Rienstra & Hirschberg 2005). The fluctuating velocity u'_{up} and pressure p'_{up} on the upstream side of the perforated plate (see figure 1) are related by

$$p'_{up} = -\mathrm{i}\rho c \,\mathrm{cotan}\left(\frac{\omega L}{c}\right) u'_{up}, \tag{3.1}$$

where ρ denotes the fresh-stream density. In the absence of the perforated plate, the duct would feature perfect quarter-wave-type eigenmodes with a pressure node and velocity anti-node at the outlet. This would correspond to $p'_{up} = 0$ in (3.1), yielding a set of eigenfrequencies defined by $f^{(n)} = (2n-1)c/4L$, where n is an integer. The corresponding modes 1, 2 and 3,... respectively refer to the quarter ($n = 1$), three-quarter ($n = 2$) and five-quarter ($n = 3$) wave eigenmodes.

It is not difficult to modify this initial description by including the perforated plate dynamics. Considering its high porosity P, the plate only slightly perturbs the duct response. Assuming that the plate is acoustically compact and that acoustic velocity perturbations remain constant in the perforations, a balance of mass through this element yields:

$$u'_{up} = Pu'. \tag{3.2}$$

The perforated-plate acoustics may be represented in terms of the bias flow aperture conductance derived by Howe (1979). In that study, the acoustic properties of the perforations are determined by the vortex shedding occurring at the downstream side of the perforations lips. In the present situation, flames are directly anchored on the plate, inhibiting vortex roll-up (see figure 1). It is thus more suitable to use another classical model derived by Melling (1973), which is based on a linearization of a Navier–Stokes description of the flow inside each individual channel. In the frequency domain, this yields a relation that links the fluctuating pressure drop across the plate and velocity fluctuations inside the holes:

$$p' - p'_{up} = \mathrm{i}\,\omega\rho l \left[1 + \frac{l_v}{r_p}(1+\mathrm{i})\right] u', \tag{3.3}$$

https://doi.org/10.1017/S0022112008003613 Published online by Cambridge University Press

where $l_v = (2\nu/\omega)^{1/2}$ stands for the viscous acoustic boundary layer thickness and ν is the kinematic viscosity. Mean flow effects are not taken into account in (3.3) but the bulk oscillation of the gas column inside the holes resulting from the unsteady pressure gradient on both sides of the plate is accounted for. Combining (3.1), (3.2) and (3.3), it is possible to link acoustic pressure and velocity at the burner outlet on the downstream side of the plate:

$$p' = \mathrm{i}\rho c \left(\frac{\omega l}{c} \left[1 + \frac{l_v}{r_p}(1+\mathrm{i}) \right] - P \operatorname{cotan}\left(\frac{\omega L}{c} \right) \right) u'. \tag{3.4}$$

3.3. *Flame transfer function*

Dynamics of flames have been studied for many years in relation to instability problems of a variety of practical systems (e.g. Crocco 1951). Some recent investigations deal with the flame transfer function analysis (Fleifil *et al.* 1996; Ducruix, Durox & Candel 2000; Schuller, Durox & Candel 2003*b*). The flame transfer function relates the response to incoming acoustic modulations in terms of heat-release-rate fluctuations as function of the excitation frequency f or angular frequency $\omega_r = \mathrm{Re}(\omega) = 2\pi f$, for a fixed input level. It is defined by the ratio of the relative variations of the global heat release rate to the relative perturbation velocity at the base of the flame:

$$\mathscr{F} = \frac{\dot{Q}'/\bar{\dot{Q}}}{u'/\bar{u}}. \tag{3.5}$$

This function may be expressed in terms of its gain $G = |\mathscr{F}|$ and phase $\varphi = \arg(\mathscr{F})$. For the case of complete premixed combustion encountered in the present configuration, the flame surface (as well as the flame light emission) is directly proportional to the heat release rate (Keller & Saito 1987). Setting A as the flame surface of one of the N flames, one can write

$$\mathscr{F}(\omega_r) = \frac{A'/\bar{A}}{u'/\bar{u}} = G(\omega_r)\, \mathrm{e}^{\mathrm{i}\varphi(\omega_r)}. \tag{3.6}$$

3.4. *Combustion noise radiation*

The sound pressure radiated by the reactive region may be deduced from classical results of combustion noise theory (e.g. Hurle *et al.* 1968; Price, Hurle & Sudgen 1968; Strahle 1978). For perfectly premixed combustion where all the reactive mixture at the burner outlet enters the reaction zone, it is possible to express the pressure perturbation as a function of the flame surface A, assuming that the laminar burning velocity S_L is constant (Abugov & Obrezgov 1978; Clavin & Siggia 1991; Joulin & Sivashinsky 1991):

$$p'(\boldsymbol{x}, t) = \frac{\rho(E-1)S_L}{4\pi|\boldsymbol{x}|} \left(\frac{\mathrm{d}A}{\mathrm{d}t} \right)_{t-\tau_x}. \tag{3.7}$$

In this expression $E = \rho_u/\rho_b$ denotes the volumetric gas expansion through the flame front. For a methane–air mixture at an equivalence ratio of 0.86 injected at ambient pressure and temperature, this ratio takes a value of 7.07 and the laminar burning velocity is $S_L = 0.31\ \mathrm{m\,s^{-1}}$. The delay $\tau_{\boldsymbol{x}} = |\boldsymbol{x}|/c$ is associated with acoustic propagation over the distance $|\boldsymbol{x}|$. This expression was recently checked for premixed flames subjected to upstream velocity modulations (Schuller, Durox & Candel 2002).

https://doi.org/10.1017/S0022112008003613 Published online by Cambridge University Press

In the present configuration, the multiple flames may be treated as a collection of N acoustic monopoles spreading over a 3 mm square mesh located at a height $h \simeq 8$ mm from the burner outlet (see figure 1). This distance h corresponds to the pinch points of the individual flame fronts during unstable operation. These points are the locations of greatest variation of volumetric consumption rate in the flame. The contributions of the different flames should be added to give the acoustic pressure p' produced by the unsteady combustion process at the burner outlet. The following development improves the crude estimate used in previous analysis (Noiray *et al.* 2006, 2007) where contributions of neighbouring flames to the net sound pressure level at the perforation outlets were omitted. In reality, the acoustical pressure at a point $\boldsymbol{x}$ results from the coherent addition of elementary contributions radiated by each flame. For large wavelengths $\lambda \gg R$ and large distances $|\boldsymbol{x}| \gg R$, the pressure field estimate used by Noiray *et al.* (2006, 2007) is justified because the collection of flames acts as a compact source zone and is considered in the far-field region. In contrast, if the field is to be evaluated at a position $\boldsymbol{x}$ in the near-field one has to sum the contributions of the different flames. This is precisely the case when $\boldsymbol{x}$ is in the the exit plane of the perforated plate. The pressure field at such a point is given by

$$p'(\boldsymbol{x}, t) = \sum_{k=1}^{N} p'(d_{\boldsymbol{x},k}, t) = \sum_{k=1}^{N} \frac{\rho(E-1)S_L}{4\pi d_{\boldsymbol{x},k}} \left(\frac{\mathrm{d}A'_k}{\mathrm{d}t}\right)_{t-\tau_{\boldsymbol{x},k}}, \tag{3.8}$$

where $d_{\boldsymbol{x},k}$ is the distance between the kth flame noise source positioned at a height h from the perforated plate and the point $\boldsymbol{x}$ located on the exit plane of the perforated plate. Observations show that under unsteady operation, flames oscillate in phase with the same amplitude (see figure 2). Equation (3.8) can thus be simplified by taking the flame surface fluctuation as the same for all flames $A'_k = A'$. Since the acoustical wavelength is much larger than the greatest distance $d_{\boldsymbol{x},k}$ (which only slightly exceeds the burner diameter) it is possible to neglect the propagation delays $\tau_{\boldsymbol{x},k}$ and assume that all the elementary contributions are in phase. This leads to the simplified expression:

$$p'(\boldsymbol{x}, t) = \frac{\rho(E-1)S_L}{4\pi D_{\boldsymbol{x}}} \left(\frac{\mathrm{d}A'}{\mathrm{d}t}\right)_t \quad \text{where} \quad \frac{1}{D_{\boldsymbol{x}}} = \sum_{k=1}^{N} \frac{1}{d_{\boldsymbol{x},k}}. \tag{3.9}$$

The function $1/D_{\boldsymbol{x}}$ is nearly constant with respect to $\boldsymbol{x}$ and a suitable estimate of the pressure field may be simply obtained by averaging this function over the plate. It is convenient to introduce an efficiency factor $\alpha = h/D = h\langle D_{\boldsymbol{x}}^{-1}\rangle$ and write the mean pressure fluctuation p' on the downstream side of the perforated plate in the form

$$p'(t) \simeq \frac{\rho(E-1)S_L}{4\pi h}\alpha \left(\frac{\mathrm{d}A'}{\mathrm{d}t}\right)_t \quad \text{where} \quad \alpha = \frac{h}{D} = h\left\langle D_{\boldsymbol{x}}^{-1}\right\rangle. \tag{3.10}$$

The coefficient α accounts for the collective effect of the N flames and defines the near-field radiation efficiency of this collection. Numerical calculations were performed to evaluate α (see figure 5). This figure shows that the amplitude of the radiated back pressure, which is proportional to α, depends on the location on the plate $\boldsymbol{x} = (x/R, y/R, 0)$. Taking the mean value integrated over the plate surface yields a factor $\alpha = 120$ (see figure 5) which indicates that near the perforated plate, the resulting acoustical pressure is 120 times that induced by a single flame over this point. If all the $N = 420$ monopole sources were at large distance from the burner outlet they would all contribute ($\alpha = N$), but here near-field effects yield a lower value

https://doi.org/10.1017/S0022112008003613 Published online by Cambridge University Press

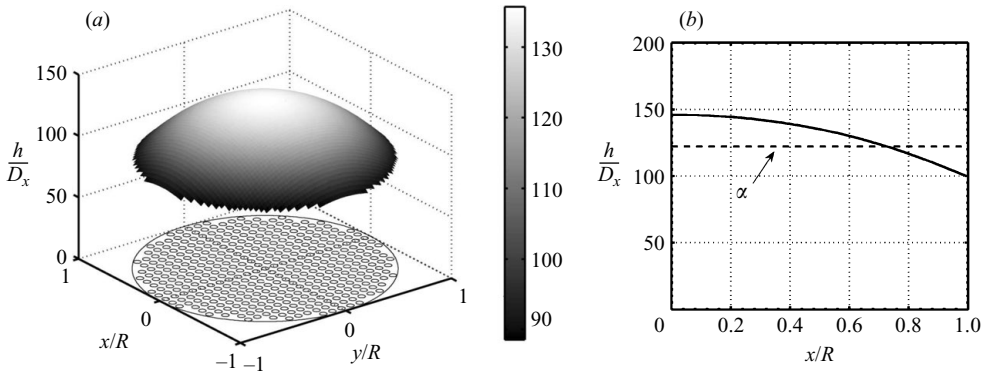


FIGURE 5. Numerical computation of the collective effect coefficient α. (*a*) A three-dimensional representation of the field h/D_x and (*b*) a profile taken along the radius in the x-direction together with α. The perforation arrangement (and thus the flame locations) is shown below the three-dimensional plot in (*a*).

$\alpha = 120$ corresponding to a reduced efficiency $120/420 \simeq 0.3$. Note that in figure 5 the ratio h/D_x is maximum, as expected, at the centre of the plate and minimum on the edges. It is also important to note that the evolution of h/D_x along a radius is smooth, justifying the approximation (3.10) used to obtain an equivalent acoustical pressure. As a final remark, the distance h is small but big enough to completely hide the discrete source distribution and yields an axisymmetrical shape. In the frequency domain, (3.10) yields

$$p' = -\mathrm{i}\omega\alpha \frac{\rho(E-1)S_L}{4\pi h} A'. \tag{3.11}$$

3.5. *Dispersion relation*

Combining (3.4), (3.6) and (3.11), gives the dispersion relation defining the system dynamics:

$$\rho c \operatorname{cotan}\left(\frac{\omega L}{c}\right) = \omega\alpha \frac{\rho(E-1)S_L}{4\pi h} \frac{\bar{A}}{\bar{u}P} G(\omega_r)\, \mathrm{e}^{\mathrm{i}\varphi(\omega_r)} + \frac{\omega\rho l}{P}\left[1 + \frac{l_v}{r_p}(1+\mathrm{i})\right], \tag{3.12}$$

which may be cast in the functional form:

$$\mathscr{H}(\omega_r + \mathrm{i}\omega_i) = \mathscr{F}(\omega_r), \tag{3.13}$$

where

$$\mathscr{H}(\omega) = \frac{4\pi h}{\alpha\omega} \frac{\bar{u}P}{(E-1)\bar{A}S_L} \frac{c}{} \left(\operatorname{cotan}\left(\frac{\omega L}{c}\right) - \frac{\omega l}{cP}\left(1 + \frac{l_v}{r_p}(1+\mathrm{i})\right)\right), \tag{3.14}$$

and $\mathscr{F}(\omega_r)$ is the flame transfer function given by (3.6). For a given set of parameters and a known flame transfer function $\mathscr{F}$, the roots ω of (3.13) with a positive imaginary part ω_i correspond to linearly unstable situations. While useful, this type of linear analysis (Noiray *et al.* 2006, 2007) cannot provide the saturation amplitude level at the limit cycle reached under unstable operating conditions. The purpose of the following sections is to investigate the nonlinear features of the resonant coupling described in this study.

https://doi.org/10.1017/S0022112008003613 Published online by Cambridge University Press

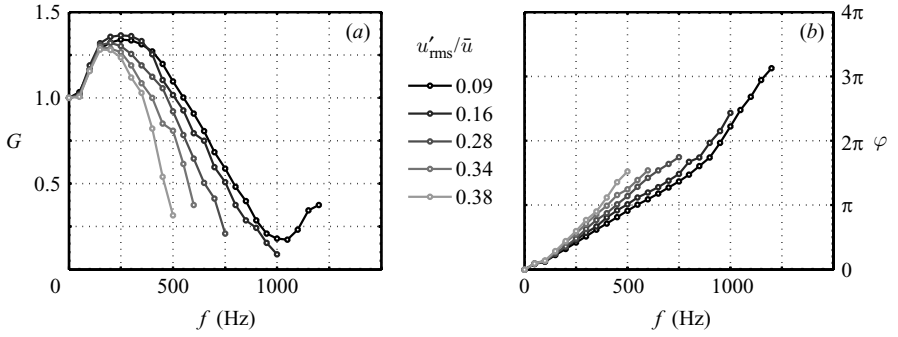


FIGURE 6. Experimental flame transfer function for different normalized driving velocity amplitudes $u'_{rms}/\bar{u}$ which are indicated in the centre. (*a*) Gain G. (*b*) Phase φ.

4. Nonlinear approach and flame describing function

Among the various theoretical methods which have been explored to take into account nonlinearities in 'acoustic–combustion' instabilities one may distinguish two general groups. The first relies on a Galerkin projection on the modes of the system and has been extensively used to investigate nonlinear acoustics as the mechanism responsible for amplitude saturation (e.g. Zinn & Lores 1972 and Culick 1994). In the second group there is a large set of models which consider that combustion is the central nonlinearity and constitutes the key element governing the system dynamics and setting limit-cycle parameters (e.g. Dowling 1997, 1999). The present analysis belongs to this second group. Unlike many previous studies which are mainly theoretical, the present approach relies on experiments to highlight the flame dynamics nonlinearities. This is accomplished in the first part of this section. It is shown that this is conveniently represented by a describing function. It is then shown that the flame describing function (FDF) can be effectively used to develop a nonlinear analysis of the system in the frequency domain through the nonlinear dispersion relation (NDR) introduced later in the paper. Theoretical results are detailed in the last part.

4.1. *Amplitude-dependent flame transfer function*

Measurements of the flame transfer function defined in (3.5) and (3.6) are carried out by simultaneously recording velocity and chemiluminescence signals in forced flow experiments (Noiray *et al.* 2006, 2007). The piston is replaced by a loudspeaker to modulate the upstream flow velocity. The velocity signal u' at the base of one of the flames is measured by means of laser Doppler velocimetry. The measurement point is located 0.7 mm above the perforation, which is a small distance compared to the flame height ($\simeq$ 7 mm). As mentioned previously OH^* chemiluminescence is proportional to the flame surface and one may write $A'/\bar{A} = I'_{OH^*}/\bar{I}_{OH^*}$ because the mixture equivalence ratio is held constant (Schuller *et al.* 2002). The OH^* light intensity is obtained by means of a photomultiplier equipped with a suitable narrowband filter. The driving frequency is swept over the range 0–1200 Hz in 50 Hz steps. For each forcing frequency f the normalized ratio between fluctuating OH^* light emission and velocity provides the gain $G(f)$ and the phase $\varphi(f)$ of the flame transfer function for a fixed level of modulation. Transfer functions measured for different driving amplitudes $|u'|$ are plotted in figure 6. The root-mean-square amplitude u'_{rms} is calculated at the fundamental frequency f determined by taking the Fourier transform of the velocity signal. The whole frequency range 0–1200 Hz cannot be completely explored because

https://doi.org/10.1017/S0022112008003613 Published online by Cambridge University Press

the driver unit efficiency is reduced in the upper frequency range for high modulation levels. We observe that for each value of the driving amplitude, the gain G and the phase φ respectively have the same general behaviour. The gain curves indicate that the flame collection acts as a low-pass filter with a visible overshoot in the low frequency range (see figure 6*a*). This filtering effect increases as the forcing level is increased. The phase (figure 6*b*) evolves in a quasi-linear fashion which is characteristic of time-delayed systems. This retarded action may be explained by introducing the time lag τ_c between the flame response and the velocity modulation at the flame base. For a constant lag the phase increases linearly with frequency $\varphi = \omega\tau_c$. This delay corresponds to the mean time required by a perturbation originating at the base of the flame to reach the entire flame surface and it may be approximated by $\beta h_f/\bar{u}$, where β is a constant factor and h_f is the flame height (Matsui 1981). Experiments indicate that β is about $1/3$ for relatively weak perturbation levels (see Ducruix *et al.* 2000). Systems featuring retarded restoring forces are susceptible to self-sustained oscillations, especially when the inverse of the time lag τ_c^{-1} is of the order of the resonant eigenfrequency f (cf. Minorsky 1962, chap. 21).

It is interesting now to examine the influence of the modulation velocity amplitude on the gain and phase of the transfer function. Figure 6(*a*), shows that both gain and phase exhibit a strong dependence on the driving velocity level. The gain G drops as the excitation velocity amplitude $u'_{\mathrm{rms}}/\bar{u}$ is increased. It is important to remember that the normalized ratio given in (3.5) is calculated using the fundamental components of the power spectral densities of light emission and velocity fluctuation signals. Power contained in the other components of the spectrum is not taken into account because we assume that harmonics do not effectively determine the self-sustained oscillation mechanism. This assumption underlies the 'describing function' or 'equivalent harmonic' formalism of control theory. In essence, the gain of the transfer function is a function of both the frequency and amplitude level of the modulating velocity.

In the present case the phase of the transfer function is also a function of the input level. According to figure 6(*b*) the slope of φ with respect to frequency increases with the relative ratio $u'_{\mathrm{rms}}/\bar{u}$, indicating that the delay τ_c increases with the input level. This mechanism may be qualitatively explained using the relation $\tau_c = \beta h_f/\bar{u}$. Under high perturbation amplitudes, the flame loses its conical shape and features an elongated cylindrical base. As a consequence, the proportionality coefficient β increases from $1/3$ to about $1/2$.

The amplitude dependence of the flame transfer function is formally expressed by writing that $\mathscr{F}$ depends explicitly on the input level $|u'|$:

$$\mathscr{F}(\omega_r, |u'|) = \frac{A'/\bar{A}}{u'/\bar{u}} = G(\omega_r, |u'|)\mathrm{e}^{\mathrm{i}\varphi(\omega_r, |u'|)}. \tag{4.1}$$

It is appropriate here to use the designation 'flame describing function' (FDF) instead of flame transfer function (FTF). This distinction is already apparent in some previous theoretical studies (e.g. Dowling 1997). Other interesting studies concerning nonlinear flame response have been carried out either by measuring the dependence of the flame transfer function on the input level (Balachandran *et al.* 2005; Bellows *et al.* 2007; Birbaud *et al.* 2007) or by analytically modelling the nonlinear flame response (Lieuwen (2005)) or by using turbulent combustion CFD (Armitage *et al.* 2006). Many of these studies also indicate that the gain drops as the input level increases, in agreement with what is observed in figure 6(*a*). However, results obtained in previous

https://doi.org/10.1017/S0022112008003613 Published online by Cambridge University Press

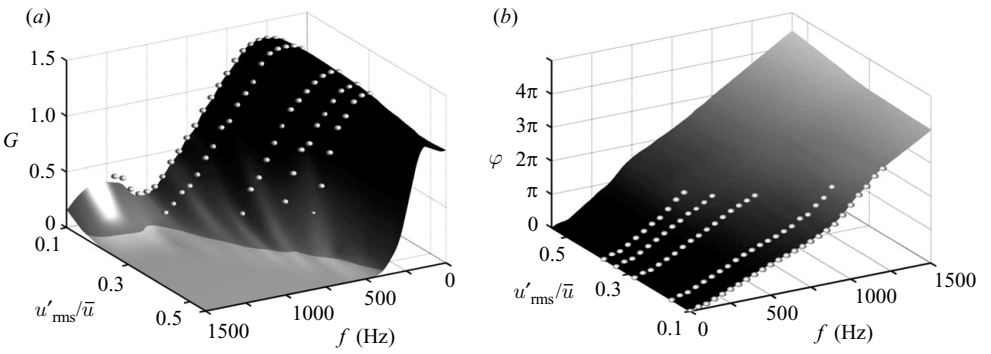


FIGURE 7. Interpolated flame describing function (FDF). Experimental data are also displayed as symbols. (*a*) Gain G. (*b*) Phase φ.

studies concerning the phase evolution as a function of the amplitude level are less straightforward than those found in the present investigation.

It is also worth noting that in the present conguration, the reaction zone is compact compared to the acoustic wavelengths considered. This is not always the case in practical systems. In such situations, it might be better to use locally defined FDF gain and phase, as recently done in the FTF framework (e.g. Martin *et al.* 2006 or Kang, Culick & Ratner (2007)).

4.2. *Nonlinear stability analysis*

The dispersion relation (3.13) has been solved by Noiray *et al.* (2006) in a linear framework using a flame transfer function which was assumed to be independent of the input velocity amplitude. It is however clear that the amplitude level changes the flame response as highlighted in the previous subsection. It is thus more appropriate to use the describing function as determined previously as a function of input level $|u'|$. The level of relative velocity fluctuation will be used instead of the absolute value and it will be expressed in terms of the root-mean-square $u'_{rms}/\bar{u}$. It is now convenient to cast (3.13) in the following fashion:

$$\mathscr{H}(\omega_r + \mathrm{i}\omega_i) = \mathscr{F}(\omega_r, |u'|), \tag{4.2}$$

where $\mathscr{F}$ is defined by (4.1). The dispersion equation now also depends on the amplitude of velocity oscillation and will be designated the nonlinear dispersion relation (NDR). It is necessary to have a well-resolved FDF in order to find the roots ω of the NDR as a function of the normalized driving amplitude $u'_{rms}/\bar{u}$. This is accomplished by interpolating the experimental FDF data and extrapolating this function where experimental samples are missing. Results of this operation are plotted in figure 7 as a function of amplitude and frequency. The interpolation is adequate in regions where data are available; it is less reliable in the high amplitude range which is not easily accessed experimentally. In this region, the FDF is simply extrapolated. This interpolated FDF is now used to develop a nonlinear analysis of the resonant coupling. This is carried out in the frequency domain, which considerably simplifies the analysis of systems with delays of the present type. The roots of the nonlinear dispersion relation are computed with a continuation algorithm.

For each duct length L and eigenmode $f^{(n)} = (2n-1)c/4L$ characterized by an integer n, equation (4.3) corresponding to the modulus of the NDR (4.2) should be solved to find the complex roots (ω_r, ω_i) as a function of the driving velocity

https://doi.org/10.1017/S0022112008003613 Published online by Cambridge University Press

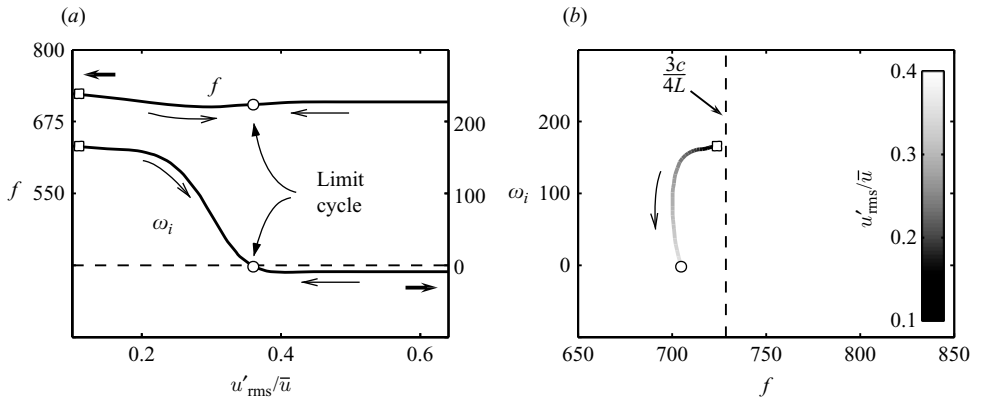


FIGURE 8. Type 1 state-space trajectory: positive growth rate ω_i from small initial perturbation amplitude (□) and vanishing growth rate ω_i (rad s^{-1}) at the limit-cycle point (○). The present trajectory corresponds to $L = 0.35$ m and to the second mode ($3c/4L$). Thin arrows with open arrowheads indicate the direction of temporal evolution of the system. Left and right bold arrows show the respective scales.

amplitude $|u'|$:

$$|\mathscr{H}(\omega_r + \mathrm{i}\omega_i) - \mathscr{F}(\omega_r, |u'|)| = 0. \tag{4.3}$$

The Nelder–Mead simplex method is used to determine the eigenfrequencies. This method provides the coordinates $(\omega_{r,\infty}, \omega_{i,\infty})$ of a local minimum of the quantity on the left-hand side of (4.3) from an initial input coordinate $(\omega_{r,0}, \omega_{i,0})$. Except for the first length L under consideration, the initial inputs $(\omega_{r,0}, \omega_{i,0})$ result from previous calculations and the root search algorithm employs a continuation methodology. The first solution of (4.3) is obtained by starting from $\omega_{r,0} = (2n-1)\pi c/(2L)$, which corresponds to a pure quarter-wave eigenfrequency, and $\omega_{i,0} = 0$. The search stops when the local minimum coordinates obtained do not change by more than 10^{-6}. It has been checked that for each iteration, the resulting local minimum $|\mathscr{H}(\omega_{r,\infty} + \mathrm{i}\omega_{i,\infty}) - \mathscr{F}(\omega_{r,\infty}, |u'|)|$ is lower than 10^{-3}.

Computations provide roots (ω_r, ω_i) as a function of $u'_{\rm rms}/\bar{u}$ for a large number of lengths L and are calculated for the first three eigenmodes of the system.

4.3. *Theoretical results*

The above algorithm is now used to examine how growth rates ω_i are affected by the input level of oscillation. As observed by Minorsky (1962), *the fundamental idea is that in all nonlinear oscillations, the amplitude and the frequency are interrelated, whereas in the linear case they are independent of each other*. It is shown here that two types of trajectories can be distinguished in an amplitude–frequency state space. A number of such trajectories are calculated and plotted for the first eigenmodes of the system.

4.3.1. *Growth rate and oscillation amplitude*

Systematic calculations of the growth rate indicate that there are two main types of trajectories in the amplitude–frequency state space. Type 1 trajectories exemplified in figure 8 feature a positive growth rate for small amplitude levels. The diagram starts at a relative amplitude of 0.1 because the flame describing function was not measured below that value. However, one may expect that very small changes will take place in the range $0 < u'_{\rm rms}/\bar{u} < 0.1$. The growth rate evolves from this initial value and eventually vanishes for a finite amplitude. The corresponding amplitude defines

https://doi.org/10.1017/S0022112008003613 Published online by Cambridge University Press

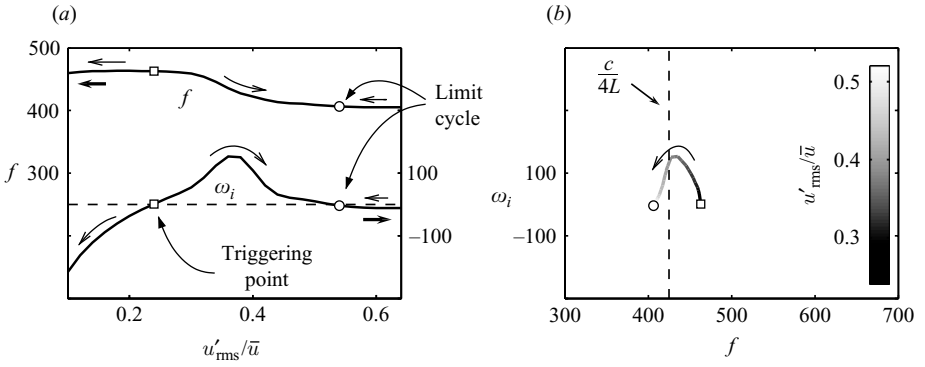


FIGURE 9. Type 2 state-space trajectory: positive growth rate from a threshold amplitude of the velocity perturbation $|u'|_0$ (□) and vanishing growth rate ω_i at the limit cycle point (○) which corresponds to the saturation amplitude $|u'|_1$. This trajectory corresponds to $L = 0.20\,\mathrm{m}$ and to the first mode ($c/4L$). Thin arrows with open arrowheads indicate the direction of temporal evolution of the system. Left and right bold arrows show the respective scales.

an oscillation state which can be maintained as a limit cycle. It is shown later that the stability of this limit cycle should also be carefully examined because nonlinear interactions with another mode may prevail and may destabilize this oscillation to another state.

Type 2 trajectories (see the example given in figure 9) feature a negative growth rate for infinitesimally small amplitudes, indicating that the corresponding operating conditions are linearly stable. For many type 2 trajectories (type 2a) the growth rate remains negative when the amplitude is below a certain threshold value $|u'|_0$ (square symbols in figure 9*a*, *b*). The growth rate then becomes positive and finally vanishes for a higher input perturbation level ($\omega_i > 0$ when $|u'|_0 < |u'| < |u'|_1$). This case exemplified in figure 9 corresponds to a linearly stable operating condition (i.e. a non-oscillating equilibrium), but to a nonlinearly unstable situation because an oscillation could be triggered by a perturbation level exceeding a certain threshold. This would then evolve into a limit cycle featuring a finite level of oscillation with an amplitude $|u'|_1$.

Other type 2 trajectories (type 2b) begin with a negative growth rate for very small amplitude levels but the growth rate remains negative for all amplitude values. The system is then linearly and nonlinearly stable. For nearly all burner sizes L investigated, there is at least one of the three first modes featuring a type 1 or type 2a trajectory. A narrow range of lengths L feature type 2b trajectories for each of the three first modes but this stable domain (non-oscillating equilibrium) is reduced to a thin band of burner sizes as shown later in the paper and in previous linear analysis (Noiray *et al.* 2006). It turns out that the combustion regime is unstable over most burner sizes.

Note also that the evolution of the frequency f as function of the incoming velocity perturbation amplitude $|u'|$ systematically occurs in the vicinity of one of the quarter-wave eigenmodes as shown in figures 8(*b*) and 9(*b*). A selected set of trajectories is plotted in figure 10. Values of ω_i are given as a function of frequency f and burner size L. They are represented in terms of the relative amplitude level by a greyscale. The plot only shows the positive branches of the trajectories. In this plot type 1 trajectories may be distinguished because they begin with very small amplitude levels shown in dark grey. It is possible to identify in this plot ranges of instability

https://doi.org/10.1017/S0022112008003613 Published online by Cambridge University Press

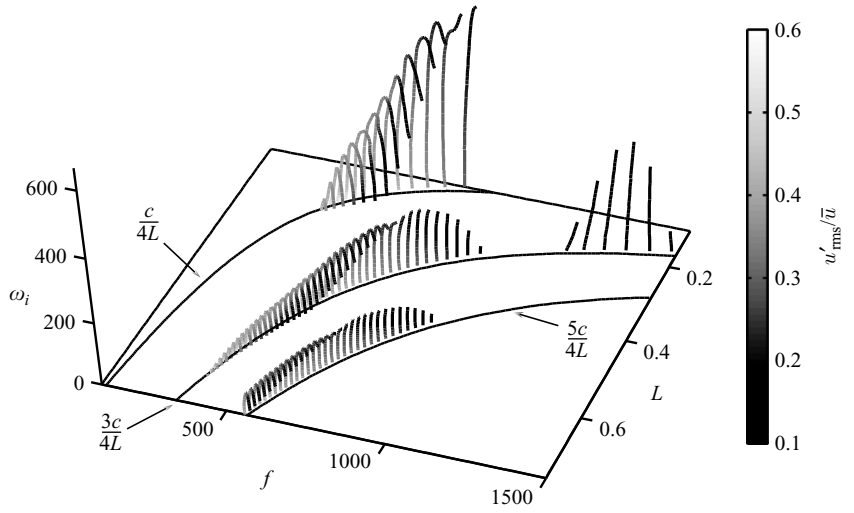


FIGURE 10. State-space trajectories determined by solving the nonlinear dispersion relation. Branches corresponding to positive growth rates are only plotted. This figure collects together type 1 and type 2a trajectories of the kind shown in figures 8(*b*) and 9(*b*). Each trajectory is marked by a greyscale level corresponding to a relative amplitude level of oscillation.

and the corresponding modes of oscillation. For certain ranges of L there are two possible trajectories featuring positive growth rates. Mode selection is in that case conditioned by the method used to reach the operating point. This is examined below by continuously changing the burner size which serves to scan the various bifurcation possibilities.

It is also informative to use the previous data to derive the bifurcation or state-space diagram displayed in figure 11. This is achieved by plotting the growth rate contours with respect to the parameter L and relative amplitude $u'_{\rm rms}/\overline{u}$.

The three modes are identified by different colours. Boundaries of the different unstable regions correspond to a vanishing value of ω_i. Inner contours pertain to positive growth rates and one observes that 'unstable' regions are mainly distinct with some overlap. This is also apparent in two of the slices plotted on the right of figure 11 showing the distribution of ω_i as a function of relative amplitude of velocity fluctuations. For a fixed cavity size $L_1 = 0.21$ m the second mode features a positive growth rate for small amplitude values, indicating that this mode is linearly unstable. The first mode on the other hand is linearly stable but nonlinearly unstable. One may infer that this mode will arise if the flow is perturbed by a finite-amplitude pulse strong enough to bring the system above the threshold. Another possibility could be to first establish the oscillation, for example at a value L_0 corresponding to a linearly unstable situation, and then continuously change L to reach L_1 the desired point of operation. It will be shown below that the two possible stable limit cycles predicted from this diagram are confirmed by experiments in which L is changed in a continuous fashion while keeping the combustion process active.

For a cavity length $L_3 = 0.6$ m the third mode is linearly unstable and we expect that this mode will appear. According to the diagram, the growth rate will eventually decrease as the amplitude increases. The type 1 trajectory crosses a type 2a trajectory corresponding to the second mode. One may expect that mode switching will take place at that point and that the oscillation frequency will jump from a value

https://doi.org/10.1017/S0022112008003613 Published online by Cambridge University Press

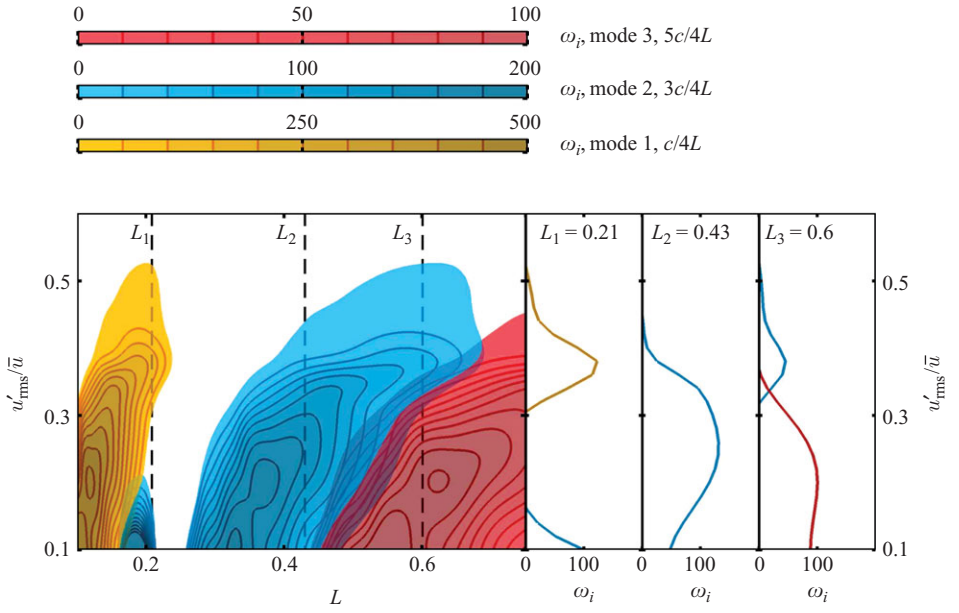


FIGURE 11. Predicted positive growth rate contours plotted as a function of burner size L and velocity fluctuation amplitude $|u'|$.

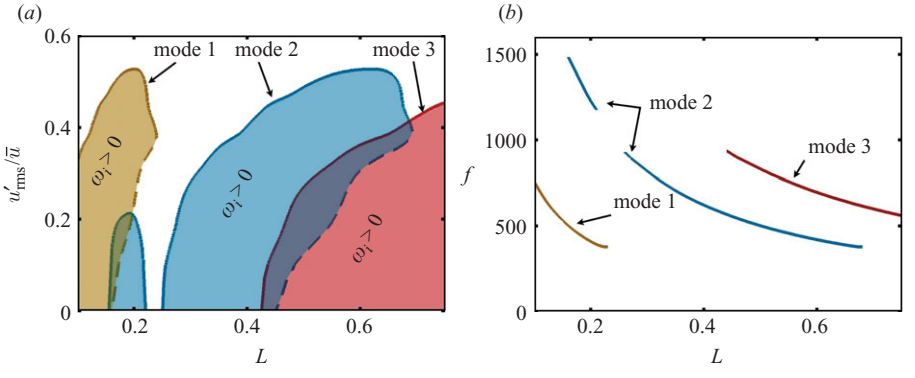


FIGURE 12. State space: (*a*) shaded regions correspond to positive growth rate ω_i. (*a*) and (*b*) Solid and dashed lines respectively designate stable and unstable equilibria ($\omega_i = 0$) of the three first modes taken independently from each other.

corresponding to the 5/4 wave mode to that of the 3/4 wave mode. This phenomenon will be exemplified below by analysing the temporal growth of oscillations for this cavity length.

The behaviour predicted for a length $L_2 = 0.43$ m is more straightforward. In this case the system is linearly unstable. The second mode arises and its final amplitude corresponds to the crossing-point of the vertical line with the $\omega_i = 0$ contour. It will be shown later that the predicted amplitude is in good agreement with that observed in the experiment.

https://doi.org/10.1017/S0022112008003613 Published online by Cambridge University Press

To complement the above interpretation it is useful to plot the previous data together with information on the frequency f. The system is characterized by its size L and its operating frequency and amplitude level. A state-space diagram is plotted in figure 12 delimiting the various positive growth rate regions which are coloured to distinguish the overlapping mode regions. An extrapolation operation has been used to extend the diagram to vanishing amplitude levels. All solid and dashed boundaries correspond to $\omega_i = 0$. In two cases the boundary features a turning point with respect to L. This critical point separates the two branches composing the boundary. The upper branch plotted as a solid line is the locus of stable limit cycles as can be seen by noting that if the system is brought to a point below this branch, the growth rate becomes positive and the amplitude increases bringing the system back to the initial equilibrium. If on the other hand the system is brought to a point located above that branch, the growth rate becomes negative and the amplitude is reduced until the initial equilibrium is reached. A similar reasoning can be used to show that the lower branches represented by dashed lines pertain to unstable limit cycles.

Figure 12(*b*) shows the oscillation frequency expected at the limit cycle. However, the stable equilibrium states predicted in these diagrams are not always reachable because the different modes may interact. Solid lines in figure 12 give the possible oscillation characteristics but the limit cycles observed experimentally also depend on the overlap between unstable regions and on initial conditions and methods used to change the bifurcation parameter L. This will be discussed and compared with experimental data below.

4.3.2. *Saturation mechanisms at limit cycles*

It is interesting to interpret what has been found previously in terms of an extension of the impedance concept. In the linear regime, one may examine the combustion response to incoming perturbations in terms of an acoustic impedance which is calculated by taking the ratio of the pressure to velocity fluctuations. When applied to the flame region, the real part of this ratio corresponds to the acoustic resistance $R_f = \mathrm{Re}(p'/u')$ and indicates the direction of energy flow. If R_f is positive, energy is dissipated in the combustion region, while a negative equivalent resistance indicates that the flames feed acoustic energy into the upstream manifold. This was used by Noiray *et al.* (2007) to examine the system stability. In that analysis the flame transfer function was determined at one fixed level of modulation typical of the values observed experimentally. It is now useful to generalize this method and make full use of the flame describing function concept. This ratio is calculated in the FDF sense by using the fundamental components of pressure and velocity fluctuations. This yields an effective impedance $Z_F = p'/u'$ which may be obtained by combining (3.11) and (4.1). The effective resistance R_F may be cast in the form

$$\left.\begin{aligned} R_F &= \mathrm{Re}(Z_F) = \mathrm{Re}\left(\frac{p'}{u'}\right) = \mathscr{N}(\omega, |u'|)\sin(\varphi(\omega_r, |u'|)) \\ \text{where}\quad \mathscr{N}(\omega, |u'|) &= \omega\alpha\frac{\rho(E-1)S_L}{4\pi h}\frac{\bar{A}}{\bar{u}}G(\omega_r, |u'|). \end{aligned}\right\} \tag{4.4}$$

where $\mathscr{N}$ is a positive factor and the resistance sign strictly depends on the FDF phase φ. Acoustic energy is fed by the unsteady flames into the upstream manifold when the resistance is negative. Perturbation amplification leading to self-sustained oscillation is only possible if the FDF phase φ belongs to the interval $[\pi, 2\pi]$ modulo 2π. This criterion written for the heat release rate and velocity oscillations at the

https://doi.org/10.1017/S0022112008003613 Published online by Cambridge University Press

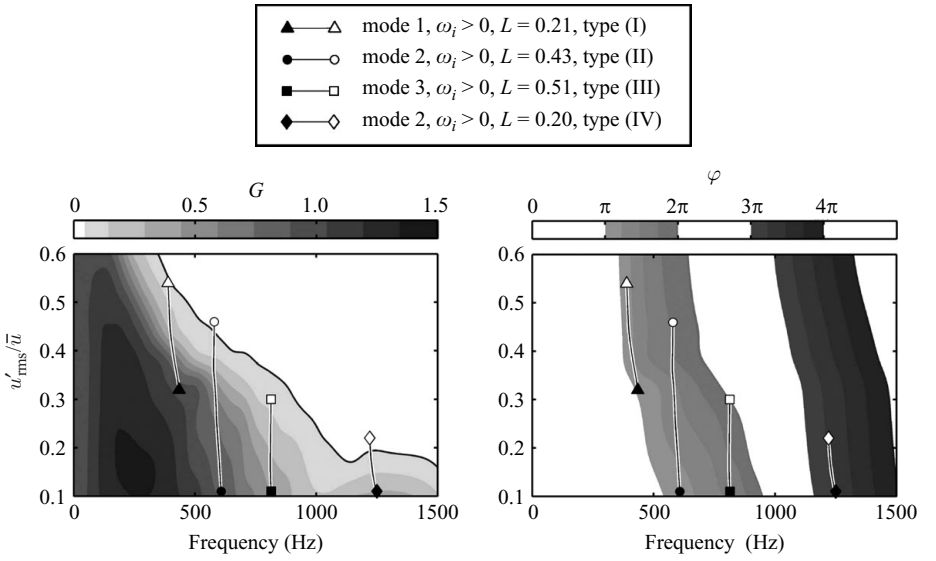


FIGURE 13. Calculated state-space trajectories superimposed on FDF contours. △, ○, □, and ◇ respectively stand for typical trajectories belonging to groups (I), (II), (III) and (IV).

burner outlet corresponds to the Rayleigh criterion, which indicates that thermo-acoustic coupling is enhanced within a system when the pressure–heat release rate phase angle is between $-\pi/2$ and $\pi/2$ modulo 2π. The proposed relation is the direct transposition of the Rayleigh criterion to unconfined systems where a compact flame is at the boundary of a resonant cavity (Schuller *et al.* 2003*a*).

An additional condition should be satisfied to trigger resonance. The acoustic energy flux released by the flames should be greater than that dissipated in the system. In the present configuration, dissipation is weak because the perforated plate, which is the main damping element, is very thin (Noiray *et al.* 2007) and the first criterion relative to φ prevails.

It is now possible to plot trajectories calculated from the NDR analysis for a given burner size and a predetermined mode in the state space together with the gain and phase of the FDF. This is done in figure 13 for a few examples. This superposition can be used to identify four different groups of trajectories.

In the first group (I) the initial point is at a finite amplitude and the system reaches a limit cycle when the gain approximately vanishes. The gain is in fact greater than zero to compensate for dissipation effects which are quite small in the present situation. The trajectory belongs to the type 2a class with an amplitude limited by the FDF gain. This trajectory is only possible when the necessary condition for the FDF phase is fulfilled (φ belongs to $[\pi, 2\pi]$ modulo 2π). This is clearly shown on figure 13(*b*) where the initial point is located on the boundary corresponding to a value of π, underlining the fact that type 2a trajectories result from an FDF phase effect because φ is amplitude dependent.

In the second group (II) the trajectory begins at a small amplitude and therefore belongs to the type 1 class. The necessary condition for the phase is satisfied along the trajectory. The limit cycle is reached when the gain nearly vanishes. There are however some deviations in practice because (i) dissipation in the system is larger than that included in the analytical model and (ii) it may also depend nonlinearly on the amplitude. As a consequence the gain will remain at a finite but low value

https://doi.org/10.1017/S0022112008003613 Published online by Cambridge University Press

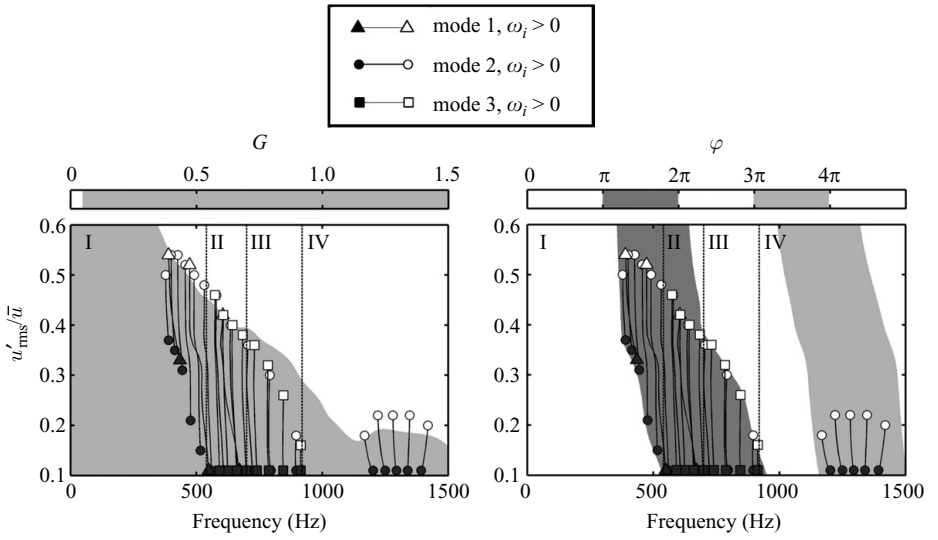


FIGURE 14. Collection of calculated state-space trajectories superimposed on FDF contours. Grey symbols feature coordinates of first positive growth rate solution of (4.2) when $|u'|$ is increased. Open symbols designate limit-cycle coordinates ($\omega_i = 0$).

to compensate these effects. For this class of trajectory, limit cycles are determined by the balance between acoustic energy gain and loss processes in accordance with a standard explanation of saturation mechanisms (e.g. Culick (2006)).

The third group (III) also includes type 1 trajectories beginning at very small amplitude levels but the limit cycle is now obtained when the phase has reached a value of 2π. In this case the gain does not vanish at the limit cycle and the saturation amplitude is fixed by the FDF phase criterion. Trajectories belonging to the fourth group (IV) are similar to those of the second group but the phase condition is now fulfilled in the second instability band $[3\pi, 4\pi]$. Having identified these different possibilities we may now plot a wider collection of tracks in the state space (figure 14). This diagram indicates that oscillating equilibria at the limit cycles are the outcome of the four different processes described above. This is independent of the mode number except for group (IV) trajectories which are only sustained by the second mode.

5. Comparison between theory and experiments

A comparison is now carried out between estimates obtained above and experimental data. It is worth noting at this point that velocity fluctuations are measured at a small distance from the plate while theoretical calculations use velocity perturbation at the flame base. The error is however quite small since the burner behaves nearly as an open-ended tube and features quarter-wave-type eigenmodes with a velocity anti-node near the plate. One can safely say that the velocity perturbation does not change by much over a short distance and that the comparison may be carried out on a quantitative basis. The velocity signal in what follows is acquired by a hot wire located 2 cm upstream of the perforated plate (see figure 1).

There are many possible ways of testing the theory. It is natural to begin by analysing time records and looking at the amplitude–frequency characteristics of an oscillation during its evolution to the limit cycle. This study, carried out by fixing the

https://doi.org/10.1017/S0022112008003613 Published online by Cambridge University Press

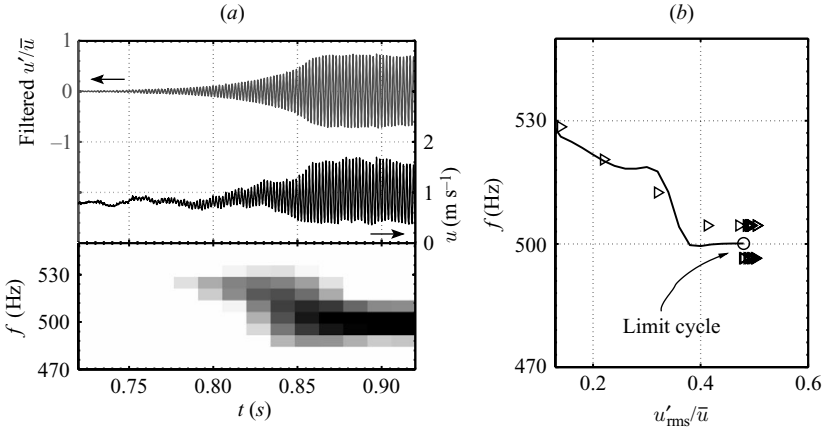


FIGURE 15. Evolution to a limit cycle. (*a*) Measurements of the flow velocity by means of a hot-wire probe placed 2 cm upstream of the perforated plate (see figure 1), L is fixed to 0.49 m. The upper box shows the temporal evolution of the total velocity and the same signal filtered and normalized by the mean velocity. The lower box displays the corresponding short-time Fourier spectral density in the frequency band of interest (470–530 Hz). Spectral resolution $\Delta f = 8$ Hz. (*b*) Comparison between NDR analysis predictions of the frequency shift as a function of the oscillation level (–○) with 'amplitude–frequency' couples (▷) extracted from the short-time Fourier analysis of the experimental signal. ○ shows the predicted saturation amplitude ($\omega_i = 0$). The evolution shown in (*b*) is similar to that illustrated in figures 8(*a*) and 8(*b*).

burner length, igniting the system and recording its evolution, is typified in figures 15 and 17. These two figures show the velocity signal detected by the hot wire which includes the mean value $\overline{u}$ and its fluctuation u'. This signal is filtered and normalized to obtain the signal of relative fluctuations $u'/\overline{u}$. A short-time Fourier analysis is used to obtain the spectral density as a function of time, which is plotted on a grey scale in the frequency band of interest. The frequency–amplitude information is then extracted from the power spectral density and plotted on figures 15(*b*) and 17(*b*) together with predictions deduced from the NDR analysis.

In figure 15, the second mode (3/4 wave) grows progressively and reaches a limit cycle at a fairly large level of fluctuation ($u'_{\rm rms}/\overline{u} \simeq 0.5$). At the same time a frequency shift is observed experimentally. The oscillation begins at 530 Hz and stabilizes around 500 Hz. This perfectly matches the theoretical prediction and an excellent agreement is obtained for the saturation amplitude. Note that this frequency shift in the vicinity of the pure quarter-wave eigenfrequencies is characteristic of a nonlinear perturbation amplification. It corresponds to the bell-shaped tracks in figure 10. Another interesting representation of this temporal evolution is given in figure 16. This phase-plane portrait is deduced from the normalized filtered velocity signal displayed in figure 15. It shows a regular evolution of the system as the trajectory begins near the origin and approaches the limit cycle.

The second case displayed in figure 17 illustrates the mode switching phenomenon. The case of a cavity length $L_3 = 0.6$ m was studied in figure 11. The calculation indicates that two trajectories cross each other and that mode switching can take place. This is indeed observed as the oscillation begins around 700 Hz and involves the third mode (5/4 wave). When the amplitude reaches a certain level the frequency suddenly drops to 440 Hz and the system switches to the second mode which then

https://doi.org/10.1017/S0022112008003613 Published online by Cambridge University Press

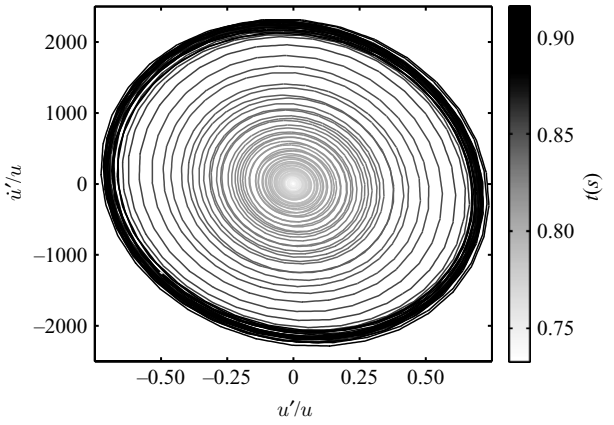


FIGURE 16. Phase-plane portrait corresponding to the filtered normalized velocity signal recorded by means of the hot wire-probe and displayed in figure 15.

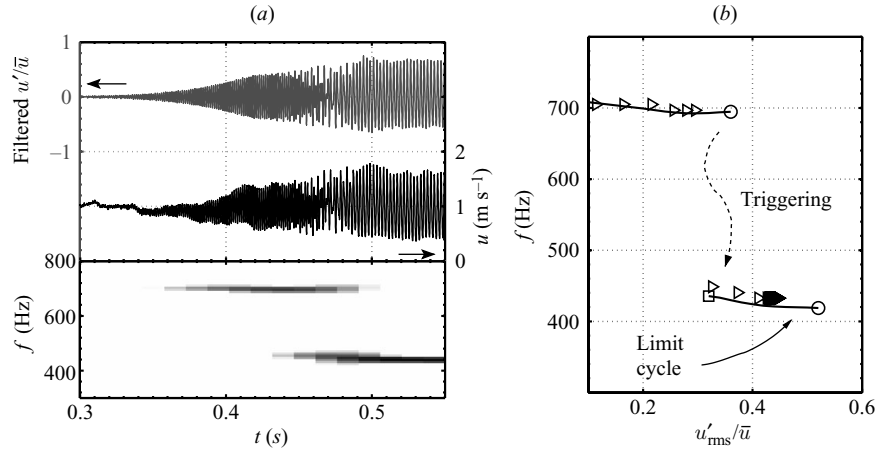


FIGURE 17. (*a*) Experimental measurements of the flow velocity by means of a hot-wire probe placed 2 cm upstream of the perforated plate (see figure 1), L is fixed to 0.6 m. The upper box shows the temporal evolution of the flow velocity and the same signal filtered and normalized by the mean velocity. The lower box displays the short-time Fourier spectral density of this signal in the frequency band of interest (400–800 Hz) with a spectral resolution of $\Delta f = 8$ Hz. (*b*) Comparison between predictions from NDR analysis (–○ and □–○) and 'frequency–amplitude' couples (▷) extracted from the short-time power spectral density. The symbols (▷) only show the dominant oscillation in the time record. Triggering of the low-frequency mode takes place when the relative velocity amplitude of the high-frequency mode reaches 0.35.

evolves to a limit cycle. Examining the details of this mechanism one finds that switching at a finite amplitude becomes possible because the second mode fulfils the phase condition and its growth rate exceeds that of the third mode at the threshold amplitude. This behaviour is typical of a nonlinearly unstable system which features a variety of eigenmodes. The corresponding phase-plane portrait given in figure 18 highlights the presence of two distinct attractors. The system reaches the first attractor but the amplitude becomes sufficiently large to allow the system to switch to the second mode and then to evolve to the second attractor.

https://doi.org/10.1017/S0022112008003613 Published online by Cambridge University Press

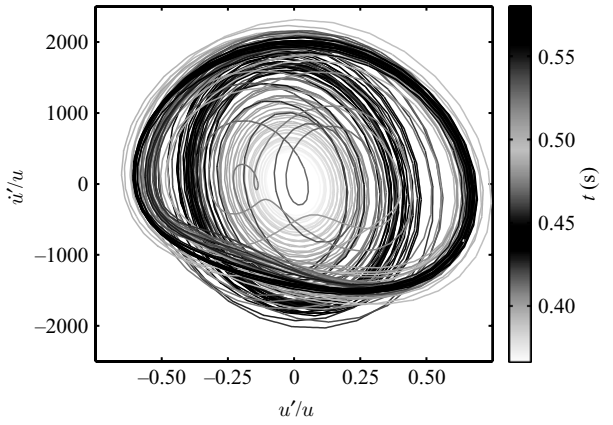


FIGURE 18. Phase-plane portrait corresponding to the filtered normalized velocity signal recorded by means of the hot-wire probe and displayed in figure 17.

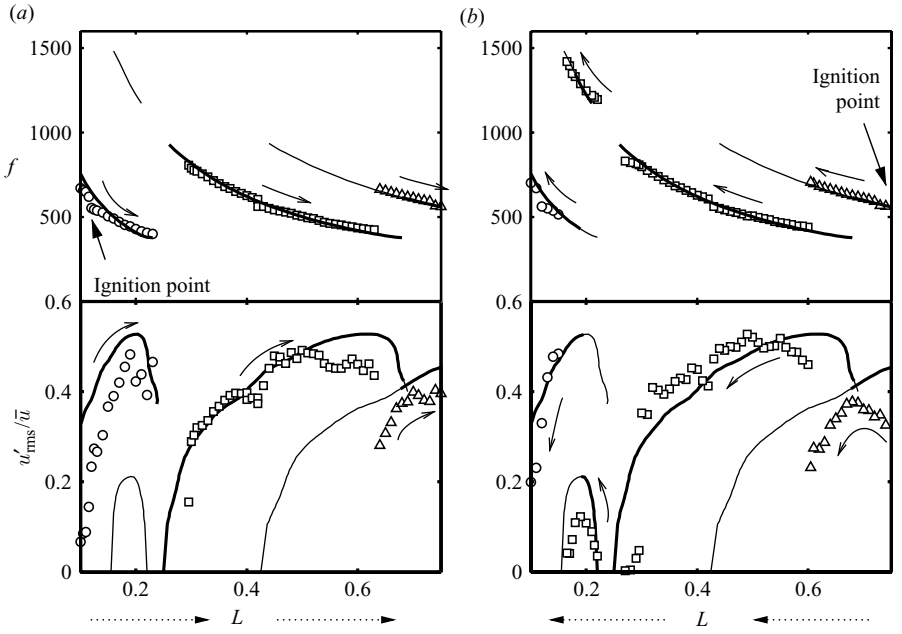


FIGURE 19. Comparison between measurements (symbols) and NDR analysis results (solid lines) of limit-cycle amplitudes and frequencies obtained by progressively changing the burner size L. Modes 1, 2 and 3 are respectively identified by ○, □ and △. Bold solid lines: limit cycle predicted by direct reading of the bifurcation diagram presented in figure 12 (reading from left to right for (*a*) and from right to left for (*b*)). Thin solid lines: stable equilibria of the different modes considered in isolation. (*a*) An experiment in which combustion is initiated for the smallest value of L, which is progressively increased while combustion is maintained. (*b*) An experiment in the reverse direction (burning is initiated at the largest burner size and L is progressively reduced).

It is interesting now to sweep the state space and compare amplitude and frequency predictions with experimental data. This is accomplished by igniting the system at an initial cavity length and continuously changing L to explore the range of accessible sizes. This can be done in two directions (see figure 19). One may begin with a low

https://doi.org/10.1017/S0022112008003613 Published online by Cambridge University Press

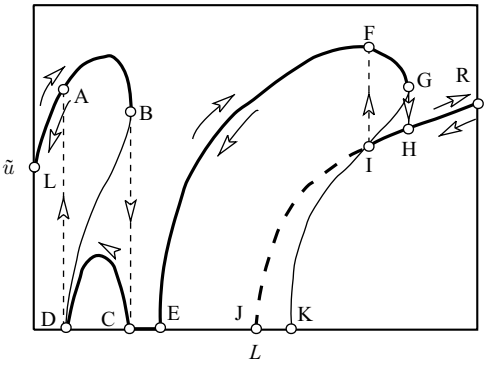


FIGURE 20. Idealized bifurcation diagram deduced from both experimental results and NDR analysis.

value of L and increase it or one may start with a large value and decrease it. Results are plotted in figures 19(*a*) and 19(*b*) respectively. Globally, the predicted limit-cycle amplitudes and frequencies are in good agreement with experimental data. Examining figure 19(*a*) shows that mode 1 appears first as expected at the ignition point which is linearly unstable (see figure 12), its amplitude increases with increasing L, reaches a maximum and decreases at the turning point ($L = 0.25$ m). There is a very narrow stable region. As L is increased the supercritical bifurcation featured by the second mode appears. The level of oscillation increases, reaches a maximum (at $L \simeq 0.5$ m) and then decreases near the turning point and the oscillation switches to the third mode.

Looking now at figure 19(*b*), the third mode is initiated first, its amplitude initially increases, then decreases at a point where mode hopping takes place ($L = 0.6$ m). The oscillation amplitude then jumps to a higher level and triggers mode 2. Decreasing L still further induces a decrease in the amplitude of this mode which vanishes at the supercritical bifurcation at $L = 0.28$ m. A stable region is reached in this way. A further decrease of L gives rise to the second mode at a fairly high frequency which persists over the predicted range of burner sizes. Mode 1 is then triggered at a higher amplitude and the oscillation then decreases from 1500 Hz to about 500 Hz.

The hysteresis phenomenon observed experimentally is fairly well retrieved by theory. This has already been discussed for figure 11 and it was indicated that for $L_1 = 21$ cm there were two possible stable oscillating equilibria for the same burner size. Notice also however some differences between predicted and measured oscillation frequencies and limit-cycle amplitudes in different regions of the diagram. This may be explained by considering that the perforated plate temperature, which increases with time, could slightly modify the flame anchoring dynamics and thus the FDF.

Finally it is interesting to combine experimental and theoretical results to propose a complete bifurcation diagram for this system showing the various branches, turning points and possible transitions between the different modes (see figure 20):

(i) (LB), (EG), (RI) and (CD) are stable limit-cycle branches corresponding to modes 1, 2, 3 and 2 respectively,

(ii) (DB) and (GK) are unstable limit-cycle branches,

(iii) (CE) corresponds to an oscillation-free stable range,

(iv) (IJ) is a stable limit-cycle branch but is not accessible because the growth rates of mode 2 oscillations bring the system to the (EF) branch,

(v) B and G are turning points, separating stable and unstable branches.

https://doi.org/10.1017/S0022112008003613 Published online by Cambridge University Press

6. Conclusion

A major result of the present study is that nonlinear combustion oscillations can be analysed by making use of the flame describing function (FDF) framework. A unified method of analysis is proposed which consists of inserting the FDF in the system dispersion relation and determining modal growth rates and modal frequencies as a function of the perturbation amplitude level. Information obtained in this way is much richer than that deduced from more standard linear stability analysis. It is then shown that one can extract amplitudes of oscillation and frequencies at the limit cycles. It would also be possible to reconstruct predicted time evolutions of the fluctuating quantities by means of these frequency-domain results.

It is also demonstrated that the mode switching (mode hopping) phenomenon which is often observed in practice can be interpreted in terms of growth rate evolutions with respect to perturbation amplitude. Jumps in frequencies are found to occur when the amplitude has reached a value at which the growth rate curve of one mode surpasses that of the mode which prevailed until that point.

Instability can also be triggered when the growth rate of a specific mode is negative for infinitesimal levels of perturbation and becomes positive for a finite amplitude level. The key element responsible for triggering and hysteresis is the FDF phase which is dependent on the driving velocity amplitude. This is specifically the case for systems with delay, such as those found in combustion, which feature bands of instability defined in terms of phase. Operating points which correspond to a linearly stable situation may become unstable because the phase of the FDF changes with the amplitude and falls in an unstable band. One may also conclude that the saturation amplitude is either defined by an equilibrium between FDF gain and system loss or by a shift in FDF phase.

These various aspects are illustrated in the case of a well-controlled system comprising an upstream manifold of variable length. It is demonstrated in particular that bifurcation diagrams showing the amplitudes of oscillation at the limit cycles are suitably well predicted with this method. This unified framework requires the determination of the FDF which can be extracted from systematic experiments or from numerical simulations and which depends on the configuration investigated.

It might also be interesting to adopt the describing function methodology to account for nonlinear dissipation mechanisms, which are weak in the simplified geometry considered in this study, but could be more important in practical applications. A dissipation describing function (DDF) could then be introduced in the analysis.

The present study is based on a bifurcation parameter related to the system geometry: the burner size L. Similar developments could be made by investigating other parameters while keeping a fixed geometry, such as the flow rate or equivalence ratio which define the flame dynamics. In such a situation to a flame describing function would have to be defined depending on the mass flow rate or equivalence ratio and fluctuating velocity amplitude. The present analysis developed in a simple configuration has more generality and could be used in more complicated situations.

This work has been partially supported by DGA. S.C. is also with Institut Universitaire de France.

REFERENCES

Abugov, D. & Obrezgov, O. 1978 Acoustic noise in turbulent flames. *Combust., Explosions Shock Waves* **14**, 606–612.

https://doi.org/10.1017/S0022112008003613 Published online by Cambridge University Press

Ananthkrishnan, N., Deo, S. & Culick, F. E. C. 2005 Reduced-order modeling and dynamics of nonlinear acoustic waves in a combustion chamber. *Combust. Sci. Technol.* **177**, 221–247.

Armitage, C. A., Balachandran, R., Mastorakos, E. & Cant, R. S. 2006 Investigation of the nonlinear response of turbulent premixed flames to imposed inlet velocity oscillations. *Combust. Flame* **146**, 419–436.

Balachandran, R., Ayoola, B. O., Kaminski, C. F., Dowling, A. P. & Mastorakos, E. 2005 Experimental investigation of the nonlinear response of turbulent premixed flames to imposed inlet velocity oscillations. *Combust. Flame* **143**, 37–55.

Balasubramanian, K. & Sujith, R. I. 2008 Non-normality and nonlinearity in combustion-acoustic interaction in diffusion flames. *J. Fluid Mech.* **594**, 29–57.

Bellows, B. D., Bobba, M. K., Forte, A., Seitzman, J. M. & Lieuwen, T. 2007 Flame transfer function saturation mechanisms in a swirl-stabilized combustor. *Proc. Combust. Inst.* **31**, 3181–3188.

Birbaud, A. L., Durox, D., Ducruix, S. & Candel, S. 2007 Dynamics of confined premixed flames submitted to upstream acoustic modulations. *Proc. Combust. Inst.* **31**, 1257–1265.

Burnley, V. S. & Culick, F. E. C. 1999 On the energy transfer between transverse acoustic modes in a cylindrical combustion chamber. *Combust. Sci. Technol.* **144**, 1–19.

Clavin, P. & Siggia, E. D. 1991 Turbulent premixed flames and sound generation. *Combust. Sci. Technol.* **78**, 147–155.

Crocco, L. 1951 Aspects of combustion instability in liquid propellant rocket motors. *J. Am. Rocket Soc.* **21**, 163–178.

Crocco, L., Grey, J. & T., Harrje D. 1960 Theory of liquid propellant rocket combustion instability and its experimental verification. *J. Am. Rocket Soc.* **30**, 159–168.

Culick, F. E. C. 1994 Some recent results for nonlinear acoustics in combustion-chambers. *AIAA J.* **32**, 146–169.

Culick, F. E. C. 2006 Unsteady motions in combustion chambers for propulsion systems. *AGARDograph*, NATO/RTO-AG-AVT-039.

Culick, F. E. C., Burnley, V. & Swenson, G. 1995 Pulsed instabilities in solid-propellant rockets. *J. Propuls. Power* **11**, 657–665.

Dowling, A. P. 1997 Nonlinear self-excited oscillations of ducted flame. *J. Fluid Mech.* **346**, 271–290.

Dowling, A. P. 1999 A kinematic model of ducted flame. *J. Fluid Mech.* **394**, 51–72.

Ducruix, S., Durox, D. & Candel, S. 2000 Theoretical and experimental determination of the transfer function of a laminar premixed flame. *Proc. Combust. Inst.* **28**, 765–773.

Fleifil, M., Annaswamy, A., Ghoneim, Z. & Ghoniem, A. 1996 Response of a laminar premixed flame to flow oscillations: a kinematic model and thermoacoustic instability results. *Combust. Flame* **106**, 487–510.

Howe, M. S. 1979 On the theory of unsteady high reynolds number flow through a circular aperture. *Proc. R. Soc. Lond.* A **366**, 205–223.

Hurle, I. R., Price, R. B., Sudgen, T. M. & Thomas, A. 1968 Sound emission from open turbulent premixed flames. *Proc. R. Soc. Lond.* A **303**, 409–427.

Jahnke, C. C. & Culick, F. E. C. 1994 Application of dynamical systems theory to nonlinear combustion instabilities. *J. Propuls. Power* **10**, 508–517.

Joulin, G. & Sivashinsky, G. I. 1991 Pockets in premixed flames and combustion rate. *Combust. Sci. Technol.* **77**, 329–335.

Kang, D. M., Culick, F. E. C. & Ratner, A. 2007 Combustion dynamics of a low-swirl combustor. *Combust. Flame* **151**, 412–425.

Keller, J. O. & Saito, K. 1987 Measurements of the combustion flow in a pulse combustor. *Combust. Sci. Technol.* **53**, 137–163.

Krebs, W., Bethke, S., Lepers, J., Flohr, P., Prade, B., Johnson, C. & Sattinger, S. 2005 Thermoacoustic design tools and passive control: Siemens power generation approaches. In *Combustion Instabilities in Gas Turbines, Operational Experience, Fundamental Mechanisms, and Modeling* (ed. T. C. Lieuwen & V. Yang). AIAA.

Lawn, C. J., Evesque, S. & Polifke, W. 2004 A model for the thermoacoustic response of a premixed swirl burner, part 1: acoustic aspects. *Combust. Sci. Technol.* **176**, 1331–1358.

Lee, J. G. & Santavicca, D. A. 2003 Experimental diagnostics for the study of combustion instabilities in lean premixed combustors. *J. Propuls. Power* **19**, 735–750.

https://doi.org/10.1017/S0022112008003613 Published online by Cambridge University Press

Lieuwen, T. 2002 Experimental investigation of limit-cycle oscillations in an unstable gas turbine combustor. *J. Propuls. Power* **18**, 61–67.

Lieuwen, T. 2005 Nonlinear kinematic response of premixed flames to harmonic velocity disturbances. *Proc. Combust. Inst.* **30**, 1725–1732.

Lieuwen, T. & Neumeier, Y. 2002 Nonlinear pressure-heat release transfer function measurements in a premixed combustor. *Proc. Combust. Inst.* **29**, 99–105.

Lieuwen, T. C. & Yang, V. (Ed.) 2005 *Combustion Instabilities in Gas Turbines, Operational Experience, Fundamental Mechanisms, and Modeling*. AIAA.

Martin, C. E., Benoit, L., Sommerer, Y., Nicoud, F. & Poinsot, T. 2006 Large-eddy simulation and acoustic analysis of a swirled staged turbulent combustor. *AIAA J.* **44**, 741–750.

Matsui, Y. 1981 An experimental study on pyro-acoustic amplification of premixed laminar flames. *Combust. Flame* **43**, 199–209.

Melling, T. H. 1973 The acoustic impedance of perforates at medium and high sound pressure levels. *J. Sound Vib.* **29**, 1–65.

Minorsky, N. 1962 *Nonlinear oscillations*. D. Van Nostrand.

Morgans, A. S. & Stow, S. R. 2007 Model-based control of combustion instabilities in annular combustors. *Combust. Flame* **150**, 380–399.

Noiray, N., Durox, D., Schuller, T. & Candel, S. 2006 Self-induced instabilities of premixed flames in a multiple injection configuration. *Combust. Flame* **145**, 435–446.

Noiray, N., Durox, D., Schuller, T. & Candel, S. 2007 Passive control of combustion instabilities involving premixed flames anchored on perforated plates. *Proc. Combust. Inst.* **31**, 1283–1290.

Paschereit, C. O., Schuermans, B., Polifke, W. & Mattson, O. 2002 Measurement of transfer matrices and source terms of premixed flames. *Trans. ASME: J. Engng Gas Turbines Power*, **124**, 239–247.

Peracchio, A. A. & Proscia, W. M. 1999 Nonlinear heat-release/acoustic model for thermoacoustic instability in lean premixed combustors. *Trans. ASME: J. Engng Gas Turbines Power* **121**, 415–421.

Poinsot, T. & Candel, S. 1988 A nonlinear model for ducted flame combustion instabilities. *Combust. Sci. Technol.* **61**, 121–153.

Poinsot, T., Veynante, D., Bourienne, F., Candel, S., Esposito, E. & Surjet, J. 1988 Initiation and suppression of combustion instabilities by active control. *Proc. Combust. Inst.* **22**, 1363–1370.

Poinsot, T., Yip, B., Veynante, D., Trouve, A., Samaniengo, J. M. & Candel, S. 1992 Active control – an investigation method for combustion instabilities. *J. Phys. Paris* III **2**, 1331–1357.

Price, R. B., Hurle, I. R. & Sudgen, T. M. 1968 Optical studies of generation of noise in turbulent flames. *Proc. Combust. Inst.* **12**, 1093–1102.

Rienstra, S. W. & Hirschberg, A. 2005 *An Introduction to Acoustics*. Eindhoven University of Technology: Report IWDE 92-06.

Roux, S., Lartigue, G., Poinsot, T. & Bérat, T. 2005 Studies of mean and unsteady flow in a swirled combustor using experiments, acoustic analysis and large eddy simulations. *Combust. Flame* **141**, 40–54.

Sattelmayer, T. 2003 Influence of the combustor aerodynamics on combustion instabilities from equivalence ratio fluctuations. *Trans. ASME. J. Engng for Gas Turbines and Power* **125**, 11–19.

Schuller, T., Durox, D. & Candel, S. 2002 Dynamics of and noise radiated by a perturbed impinging premixed jet flame. *Combust. Flame* **128**, 88–110.

Schuller, T., Durox, D. & Candel, S. 2003*a* Self-induced combustion oscillations of laminar premixed flames stabilized on annular burners. *Combust. Flame* **135**, 525–537.

Schuller, T., Durox, D. & Candel, S. 2003*b* A unified model for the prediction of laminar flame transfer functions : comparisons between conical and v-flame dynamics. *Combust. Flame* **134**, 21–34.

Searby, G. & Rochwerger, D. 1991 A parametric acoustic instability in premixed flames. *J. Fluid Mech.* **231**, 529–543.

Strahle, W. C. 1978 Combustion noise. *Prog. Energy Combust. Sci.* **4**, 157–176.

https://doi.org/10.1017/S0022112008003613 Published online by Cambridge University Press

Wicker, J. M., Greene, W. D., Kim, S. & Yang, V. 1996 Triggering of longitudinal combustion instabilities in rocket motors: Nonlinear combustion response. *J. Propul. Power* **12**, 1148–1158.

Wu, X. S., Wang, M., Moin, P. & Peters, N. 2003 Combustion instability due to the nonlinear interaction between sound and flame. *J. Fluid Mech.* **497**, 23–53.

Yang, V., Kim, S. I. & Culick, F. E. C. 1990 Triggering of longitudinal pressure oscillations in combustion chambers. 1. nonlinear gas dynamics. *Combust. Sci. Technol.* **72**, 183–214.

Zinn, B. T. & Lores, M. E. 1972 Application of galerkin method in solution of nonlinear axial combustion instability problems in liquid rockets. *Combust. Sci. Technol.* **4**, 269.

https://doi.org/10.1017/S0022112008003613 Published online by Cambridge University Press